



Cobalt-doped carbon nanodots as an interfacial modifier for efficient solar-driven water splitting

Jingyi Lin ^{a,b}, Runlu Liu ^a, Xin Li ^c, Yixin Zhao ^c, Lingti Kong ^a, Yao Li ^a, Shenmin Zhu ^{a,*}, Lianzhou Wang ^{b,*}

^a State Key Laboratory of Metal Matrix Composites, School of Materials Science and Engineering, Shanghai Jiao Tong University, Shanghai 200240, China

^b Nanomaterials Centre, School of Chemical Engineering and Australian Institute for Bioengineering and Nanotechnology, The University of Queensland, QLD 4072, Australia

^c School of Environmental Science and Engineering, Shanghai Jiao Tong University, Shanghai 200240, China



ARTICLE INFO

Keywords:

Carbon nanodots
Water splitting
Photoanode
Bismuth vanadate
Interface modification

ABSTRACT

Photoelectrochemical water splitting with bismuth vanadate (BiVO_4) photoanodes is a promising strategy for solar-driven hydrogen production. However, the unfavorable interfacial charge behavior causes severe charge recombination and photocorrosion issue of BiVO_4 . Herein, cobalt-doped carbon nanodots (CoCDs) are employed for efficient charge extraction due to Co impurity level, which form band alignment with BiVO_4 , as well as accelerate surface reaction. As a result, the obtained CoCDs/BVO photoanode demonstrates an outstanding photocurrent density of 5.26 mA/cm^2 at 1.23 V vs. reversible hydrogen electrode under AM 1.5 G illumination, superior to most BiVO_4 photoanodes with cocatalysts. Carbon nanodots turn out to be an excellent matrix to activate and stabilize Co atoms and tightly anchor onto BiVO_4 , which makes them good interfacial modifier. This work paves an avenue for the optimization of semiconductor/liquid interface and the application of carbon nanomaterials in photoelectrodes.

1. Introduction

Confronted with the enormous demands for clean energy, photoelectrochemical (PEC) water splitting for hydrogen production is rising as an attractive technology in recent years [1,2]. A PEC system can capture sunlight to drive chemical reactions and store solar energy in the form of chemical bonds. The key component of a PEC system is semiconductive photoelectrodes and the PEC process happened on the photoelectrodes can be divided into three steps: light harvesting, charge separation and surface reaction [3]. Semiconductor/liquid interface is the dominant region where the reactions take place and the space charge region near this interface drives the electron-hole separation [4]. The optimization of the semiconductor/liquid interface has a great impact on the activity and stability of the photoelectrodes [5]. For example, monoclinic bismuth vanadate (BiVO_4) has been regarded as a promising material for photoanodes because of its suitable band gap ($\sim 2.4 \text{ eV}$) and favorable band edge positions [6]. However, the experimental photocurrent density of BiVO_4 photoanodes is restricted by its unfavorable interfacial charge behavior for the oxygen evolution reaction (OER).

What's more, accumulated photogenerated holes at the interface can also cause photocorrosion and inhibit the stability of BiVO_4 photoanodes [7,8].

To promote the performance of BiVO_4 photoanodes, charge carriers should be able to be extracted from the interface and participate into the reaction efficiently. Heterojunction construction is a good method to extract electrons by band alignment. Recently, Zhou and colleagues found carbon nanodots (CDs) could improve light harvesting and form heterojunction with BiVO_4 [9]. Wang *et al.* also reported that grafting laser-generated CDs on the BiVO_4 surface could effectively accelerate interfacial transportation of charge carriers [5]. Flexible electronic structure of CDs can modulate the charge injection/extraction energy barrier [10] and act as a photosensitizer [11]. Their abundant surface functional groups serve as anchors onto the surface of semiconductors to be charge transfer pathway, which makes them an excellent interfacial modifier for photoanodes. What's more, carbon nanodots have also been reported as a multifunctional electrocatalyst, which distinguishes them from $\text{WO}_3/\text{BiVO}_4$ [12] or $\text{g-C}_3\text{N}_4/\text{BiVO}_4$ heterojunctions [13] but is always neglected previously. Synthesis of CDs can be realized by

* Corresponding authors.

E-mail addresses: smzhu@sjtu.edu.cn (S. Zhu), l.wang@uq.edu.au (L. Wang).

pyrolysis or carbonization of various small organic molecules [14], such as citric acid [15,16], glucose [17], tannic acid [5]. The functional groups and heteroatoms inherited from precursors can tune the physicochemical properties of CDs, which endows them good diversity for wide catalysis applications [14]. For example, Zhi's group fabricated carbon nanodots with abundant oxygen-containing functional groups, which was applied as a highly efficient electrocatalyst for two-electron oxygen reduction reaction [17]. Kang *et al.* demonstrated that CDs modified with amidogen and phosphorus species possessed catalysis activity for both oxygen evolution and reduction reactions [18]. Therefore, CDs are promising to be a multifunctional interfacial modifier, which can assist charge separation, as well as accelerate surface reaction through appropriate design of chemical composition and band structure.

For electrocatalytic oxygen evolution reaction (OER), transition-metal (e.g., Co, Fe, Ni) composite materials have been extensively studied as effective and low-cost catalysts [19], but their stability has been challenged because of the dissolution of transition metal atoms [20]. Carbon nanomaterials are considered as ideal substrates to stabilize metal atoms [21], thus form robust electrocatalysts for OER. What's more, heteroatoms can modulate the electronic configuration of carbon nanodots and the cooperation between carbon matrix and metal dopants can boost the activity of metal sites [22]. In this context, through suitable composition tuning, transition-metal doped carbon nanodots are supposed to be a promising modifier to photoelectrodes for simultaneously improvement of charge separation and surface reaction, but have not yet been explored.

Herein, cobalt-doped carbon nanodots (CoCDs) has been designed as a bifunctional interfacial modifier for BiVO₄ photoanodes. Upon doping, CoCDs are endowed with high dispersity, favorable band structure and catalysis capability, therefore CoCDs turn out to be an excellent cocatalyst and hole extractor. On the other hand, the carbon matrix stabilizes Co atoms and tightly anchors onto BiVO₄. The BiVO₄ photoanode decorated by CoCDs (CoCDs/BVO) exhibits an excellent photocurrent density of 5.26 mA/cm² at 1.23 V_{RHE} under AM 1.5 G illumination and a maximum applied bias photon-to-current efficiency (ABPE) of 2.04% at 0.61 V_{RHE}. Detailed investigations reveal that such a performance result from a boosted charge separation efficiency and an ultrahigh charge transfer efficiency approaching to 100%, owing to the well-aligned band structure between CoCDs and BVO and the efficient OER activity of CoCDs. The performance of CoCDs/BVO ranks among the best BiVO₄ photoanodes coupled with cocatalysts, thus qualifies cobalt-doped CDs as an excellent interfacial modifier for effective and robust photoanodes.

2. Experimental methods

2.1. Materials

Bi(NO₃)₃·5 H₂O (99%, AR), citric acid (99.5%, AR) and Co(NO₃)₂·6 H₂O (99%, AR) were purchased from Sinopharm Chemical Reagent Co., Ltd. KI (99%, AR), ethanol (99.5%, AR), *p*-benzoquinone (98%, CP), dimethyl sulfoxide (99.5%, AR), vanadyl acetylacetone (99%, AR) and NaOH (96%, AR) were purchase from Shanghai Aladdin Biochemical Technology Co., Ltd. All chemicals were used without further purification.

2.2. Synthesis of carbon nanodots (CDs) and cobalt-doped carbon nanodots (CoCDs)

The CDs aqueous solution was prepared by a one-step hydrothermal method. 1050 mg of citric acid was dissolved in 10 mL of deionized water and stirred for 1 h, which was transferred into a 100 mL Teflon-lined stainless-steel autoclave and heated at 200 °C for 8 h. After cooling to room temperature, the product was filtered with PES Millipore membrane with a pore diameter of 0.22 μm and further dialyzed with a dialysis bag (MW 1000) for 24 h.

The CoCDs aqueous solution was prepared using 1050 mg of citric acid and 145.5 mg of Co(NO₃)₂·6 H₂O as precursor. The subsequent treatment was same as that of CDs.

2.3. Preparation of BiVO₄ (BVO), CoCDs/BVO and CDs/BVO electrodes

Before synthesis, the fluorine-doped tin oxide (FTO) pieces were ultrasonic cleaned in water, acetone and ethanol in sequence for 20 min and then dried at 60 °C. The electrodeposition process of BVO electrodes was carried out according to the previous literature [23]. The CoCDs/BVO electrodes were obtained by dropping 100 μL of CoCDs solution onto BVO electrodes and drying at 60 °C. The drop coating step was repeated for three times. For CDs/BVO electrodes, the CDs solution was used instead.

2.4. Photoelectrochemical measurement

All the PEC measurements were performed on an electrochemical workstation (CHI660E, CH Instruments, Inc.) using a three-electrode configuration. An Ag/AgCl (saturated KCl electrolyte) electrode and a Pt foil were used as reference electrode and counter electrode, respectively. 1 M potassium borate solution (1 M KBi, pH=9.7) was used as the electrolyte. A 300 W Xe lamp (CEL-HXUV300, CEAULIGHT Co. Ltd.) with an AM 1.5 G filter was illuminated from the back side of the samples as the light source. The light intensity on the samples was adjusted to 100 mW/cm² by a photoradiometer (PL-MW 2000, Perfectlight Technology Co. Ltd.).

Photocurrent (J)-potential (V) curves were measured by linear sweep voltammetry (LSV) method with applied voltage of 0.1~1.7 V_{RHE} and a scan rate of 10 mV/s. Electrochemical impedance spectrum (EIS) was obtained with an amplitude of 5 mV and a frequency range of 0.01 Hz~100 kHz at the open circuit potential in the dark. Mott-Schottky analysis was performed by sweeping the range of 0.1~0.7 V_{RHE} with an AC frequency of 1 kHz and an amplitude of 5 mV under dark condition.

2.5. Characterization

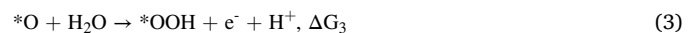
The morphology was characterized by scanning electron microscopy (SEM, JSM-6360LV), transmission electron microscopy (TEM, TALOS F200X) and atomic force microscopy (AFM, MFP-3D). Scanning transmission electron microscope-high angle angular dark field (STEM-HAADF) images were taken by Hitachi HF5000 with spherical aberration corrector. Zeta potentials were determined by a DLS instrument (Malvern Mastersizer 2000). Photoluminescence (PL) spectra were acquired at room temperature on a Shimadzu RF-5301PC fluorescence spectrophotometer. XRD patterns of the samples were recorded on a Rigaku D/max 2550VL/PC system, using Cu K α radiation. Ultraviolet-Visible (UV-Vis) absorption spectra and Fourier transform infrared (FTIR) spectra were recorded by PerkinElmer Lambda 750 S UV-Vis-NIR spectrophotometer and Thermo Scientific Nicolet 6700 spectrometer. X-ray photoelectron spectra (XPS) were collected on an Thermo Scientific K-Alpha X-ray photoelectron spectrometer with an Al K α ($h\nu = 1486.8$ eV) radiation source. All the binding energy was calibrated with C 1s (284.8 eV) as reference. The contact angle was recorded by a Drop Shape Analyzer system (DSA100, KRÜSS, Germany).

2.6. Computational details

All density functional theory (DFT) calculations were conducted by using the Vienna ab initio simulation package (VASP) [24]. The generalized gradient approximation (GGA) of the Perdew-Burke-Ernzerhof (PBE) functional was employed to describe the exchange-correlation interaction. All calculations were performed at the Γ-point with spin polarization. An energy cutoff for plane-wave of 650 eV was used, and convergence criteria of 1×10^{-5} eV for electronic

relaxation and of 0.03 eV/Å for ionic relaxations were adopted.

For CDs and CoCDs, carbon models with 14 hexagonal rings capped with H atoms were constructed as the previous literature [17]. The oxygen evolution reaction (OER) process can be divided into four steps:



where “*” refers to an active site on the catalyst and *O, *OH and *OOH are adsorbed intermediates [25].

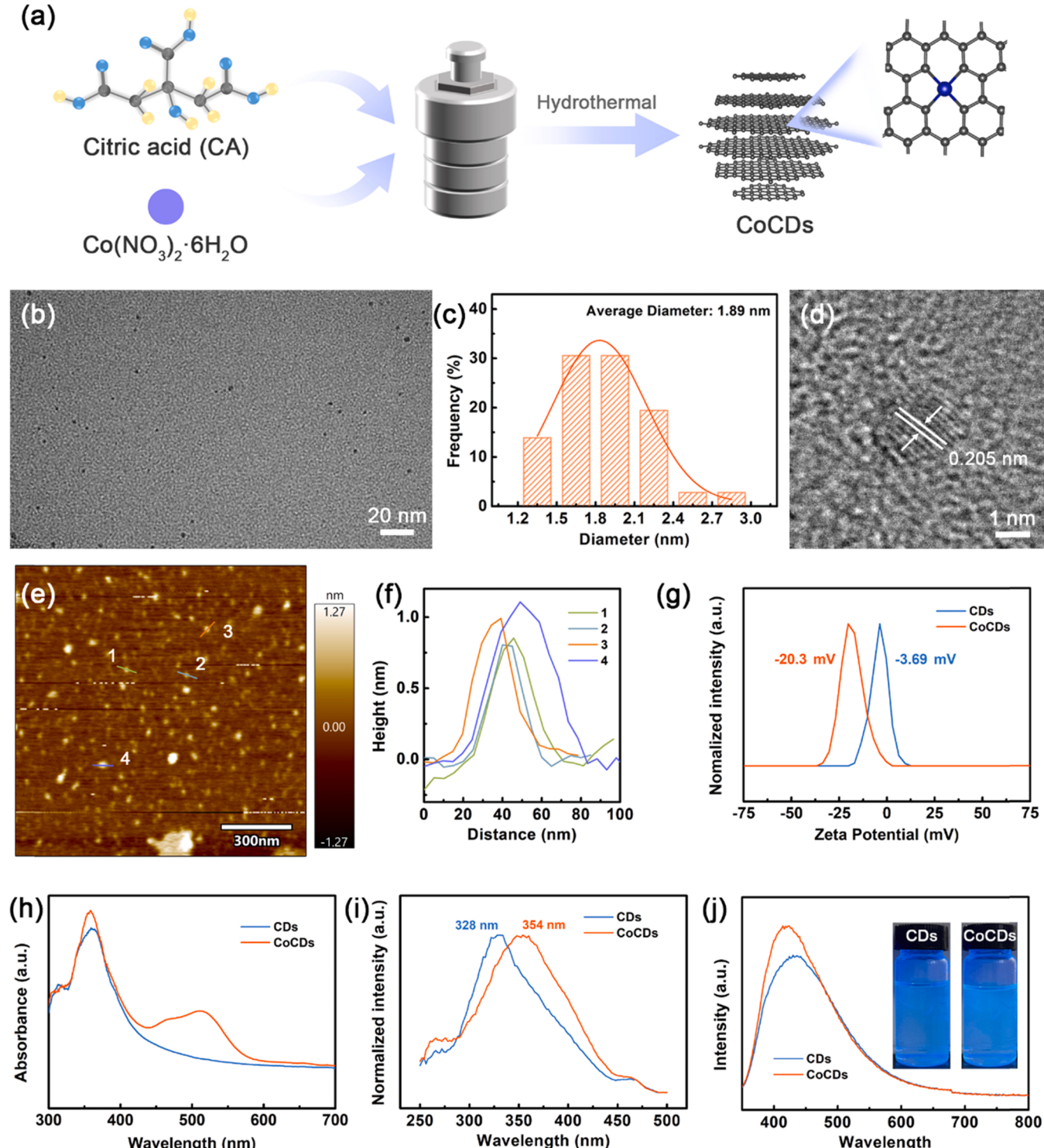


Fig. 1. (a) Schematic illustration of the preparation of CoCDs. (b) TEM image, (c) the size distribution and (d) HRTEM image of CoCDs. (e) AFM image of CoCDs and (f) the corresponding height analysis performed along the line shown in (e). (g) Zeta potential and (h) UV-Vis spectra of CoCDs and CDs. (i) Photoluminescence excitation (PLE) spectra of CDs and CoCDs with the emission at 350 nm. (j) Photoluminescence emission spectra of CDs and CoCDs with the excitation wavelength at 340 nm. (Insets: Optical images of luminescence of CDs and CoCDs under irradiation of an ultraviolet lamp.).

The Gibbs free energy change for the OER process is $\Delta G = E_{abs} + \Delta E_{ZPE} - T\Delta S + \Delta U(0 \rightarrow T)$, where E_{abs} , ΔE_{ZPE} and ΔS are the adsorption energy of intermediate, change in zero-point energy and entropy change of the reaction, respectively. ΔU is the internal energy difference between 0 K and T (298.15 K). The thermal correction for adsorbate was calculated by using the VASPKIT package [26] and the overpotential is defined as $\eta = \max\{\Delta G_1, \Delta G_2, \Delta G_3, \Delta G_4\}/e - 1.23V$.

For the calculations of CoCDs/BVO and CDs/BVO, a $3 \times 3 \times 2$ supercell of the BiVO_4 (001) slab was constructed from the primitive cell of monoclinic- BiVO_4 with a vacuum region of 30 Å in thickness, leading to 216 atoms in the slab model. To account for the van der Waals (vdW) interactions, the DFT+D3 method was employed [27]. Here the energy cutoff for plane-waves was 400 eV and the convergence criteria are 1×10^{-4} eV and 0.1 eV/Å for electronic and ionic relaxations, respectively.

3. Results and discussion

3.1. Cobalt-doped carbon nanodots (CoCDs)

The synthesis of cobalt-doped carbon nanodots (CoCDs) and pure carbon nanodots (CDs) was achieved by a facile hydrothermal method. As sketched in Fig. 1(a), $\text{Co}(\text{NO}_3)_2 \cdot 6 \text{ H}_2\text{O}$ and citric acid (CA) were selected as the cobalt source and carbon source, respectively. During the hydrothermal reaction, CA molecules dehydrate and form graphitic structure [28]. In the meanwhile, Co atoms are wrapped into the carbon skeleton as dopants. The particle sizes of the resultant carbon nanodots were first examined by transmission electron microscope (TEM). As shown in Fig. S1, CDs have an average diameter of ~ 1.88 nm. Upon cobalt doping, the particle size remains similar. As given in Fig. 1(b) and (c), CoCDs have an average diameter of 1.89 nm. High-resolution TEM (HRTEM) image of CoCDs in Fig. 1(d) shows an interlayer spacing of 0.205 nm, corresponding to the (100) facet of graphite [18], which indicates the good crystallinity of carbon nanodots upon doping. Atomic force microscope (AFM) image of CoCDs in Fig. 1(e) further exhibits that CoCDs have an average height of ~ 0.94 nm (Fig. 1(f)), while CDs have a slightly higher height of ~ 1.24 nm (Fig. S2). What's more, it can be observed from the AFM images that CDs suffer from more severe particle aggregation, while CoCDs distribute uniformly. The zeta potentials of CoCDs and CDs are -20.3 mV and -3.69 mV, respectively (Fig. 1(g)). Both of them have negative charge on the surface, originating from the surface groups. The more negative zeta potential of CoCDs indicates their better stability and dispersity due to the stronger repulsive force between the particles [29], consistent with the observation from AFM images. Therefore, the cobalt dopant provides carbon nanodots higher dispersity without destroying the original structure.

The optical properties of carbon dots can be affected by their composition [30]. As shown in Fig. 1(h), the UV-Vis absorption spectrum of CDs exhibits only one peak centered at 360 nm, corresponding to the $\pi-\pi^*$ transition from the sp^2 skeleton and the $\text{n}-\pi^*$ transition from oxygen-containing groups [31,32]. By contrast, in the UV-Vis spectrum of CoCDs, in addition to the peak at 358 nm, a broad absorption peak between 440 nm and 580 nm appears, which may result from the absorption of transition between Co impurity level and molecular orbital of carbon nanodots [32]. The photoluminescence excitation (PLE) spectra of CDs and CoCDs are given in Fig. 1(i). The PLE spectrum of pure CDs shows a peak at 328 nm (3.78 eV), which can be considered as the transition between the highest occupied molecular orbital (HOMO) and the lowest unoccupied molecular orbital (LUMO) [33]. In comparison, the peak of CoCDs exhibits a red shift to 354 nm (3.50 eV), which further proves the existence of Co impurity level between original HOMO and LUMO. When the excitation wavelength increases from 340 to 500 nm, a gradual red shift from about 420–560 nm in the emission peaks of CDs and CoCDs is observed (Fig. S3). This excitation-dependent property results from multiple luminescence centers, which is a feature of carbon nanodots [34,35]. Moreover, under the same excitation

wavelength at 340 nm, CDs and CoCDs show photoluminescence emission peak in the blue light region (Fig. 1(j)), therefore, blue fluorescence emission can also be observed from both CDs and CoCDs under the irradiation of an ultraviolet lamp (insets in Fig. 1(j)).

3.2. BiVO_4 electrodes coated by CoCDs

The as-prepared carbon nanodots were then coated onto BiVO_4 electrodes (BVO) that were first synthesized by an electrodeposition and calcination method. Bare BiVO_4 electrodes have a typical nanoporous morphology (Fig. S4(a)). The CoCDs/BVO and CDs/BVO electrode still maintains the original morphology of BVO, as shown in Figs. 2(a) and S4(b). However, small particles can be observed on the surface of BiVO_4 particles in the TEM image in Fig. 2(b). CoCDs distributed uniformly on the surface of BVO owing to the strong inter-particle repulsive force (Fig. 1(g)). The HRTEM image in Fig. 2(c) reveals a lattice spacing of 0.46 nm in the matrix, corresponding to the (110) plane of monoclinic BiVO_4 . The diameter of attached particles is about 2 nm, which can be assigned to the carbon nanodots. Scanning transmission electron microscope-energy dispersive spectroscopy (STEM-EDS) mapping in Fig. S5 exhibits the uniform distribution of Co on BVO, indicating the distribution of CoCDs.

Due to the low content of carbon nanodots, the X-ray diffraction (XRD) patterns of both CoCDs/BVO and CDs/BVO in Fig. 2(d) only exhibit the diffraction peaks of monoclinic BiVO_4 and FTO substrate. X-ray photoelectron spectroscopy (XPS) measurements were employed to verify the existence of carbon nanodots. The high-resolution C 1s spectra in Fig. 2(e) can be deconvoluted into three peaks located at about 284.8 eV, 286.5 eV and 288.4 eV, which correspond to C-C, C-O and C=O, respectively. Compared with bare BVO, the ratios of C-O and C=O peaks increase obviously in CoCDs/BVO and CDs/BVO photoanodes, which originate from the oxygen-containing functional groups (e.g., carbonyl groups and carboxyl groups) in the carbon nanodots. What's more, as listed in Table S1, CoCDs/BVO contains more C-O species, while CDs/BVO contains more C=O species. The Fourier transform infrared (FTIR) spectra in Fig. 2(f) further confirm this difference. Both CDs/BVO and CoCDs/BVO shows absorption band at about $1560 \text{ cm}^{-1} \sim 1530 \text{ cm}^{-1}$, corresponding to the vibration of conjugated aromatic skeleton [30]. In addition, the FTIR spectrum of CDs/BVO exhibits absorption peak at 1700 cm^{-1} , corresponding to the vibration of C=O [5], while the peak at 1397 cm^{-1} in the spectrum of CoCDs/BVO can be attributed to C-O [32,36]. The coordination difference may result from the incorporation of Co atoms, which may break the carbon-oxygen double bonds and form C-O-Co structure.

3.3. Photoelectrochemical (PEC) performance of CoCDs/BVO

The photoelectrochemical (PEC) water splitting performance was evaluated in 1 M potassium borate buffer solution (1 M KBr, pH=9.7) under AM 1.5 G illumination. Cobalt-doped carbon nanodots can dramatically enhance PEC performance of BVO photoanode. As shown in Fig. 3(a), the photocurrent density of CoCDs/BVO reaches 5.26 mA/cm^2 at 1.23 V vs. reversible hydrogen electrode (RHE), which is 3.9-fold of that of bare BVO (1.34 mA/cm^2) and 2.5-fold of the photocurrent density of CDs/BVO (2.10 mA/cm^2). What's more, the onset potential of BiVO_4 negatively shifts from 0.40 V_{RHE} to 0.21 V_{RHE} upon the coating of CoCDs, which indicates its capability to accelerate surface reaction. The applied bias photon-to-current efficiency (ABPE) can be calculated from the corresponding J-V curves. As illustrated in Fig. 3(b), the maximum ABPE of BVO is merely 0.29% at 0.84 V_{RHE}. However, the maximum ABPE of CoCDs/BVO reaches 2.04% at a lower potential of 0.61 V_{RHE}, which is 7.0 times as high as that of bare BVO and much higher than that of CDs/BVO (0.64% at 0.73 V_{RHE}). As compared in Table S2, the performance of CoCDs/BVO is superior to most reported BiVO_4 photoanodes modified by cocatalysts.

As known, the PEC water oxidation process is comprised of three

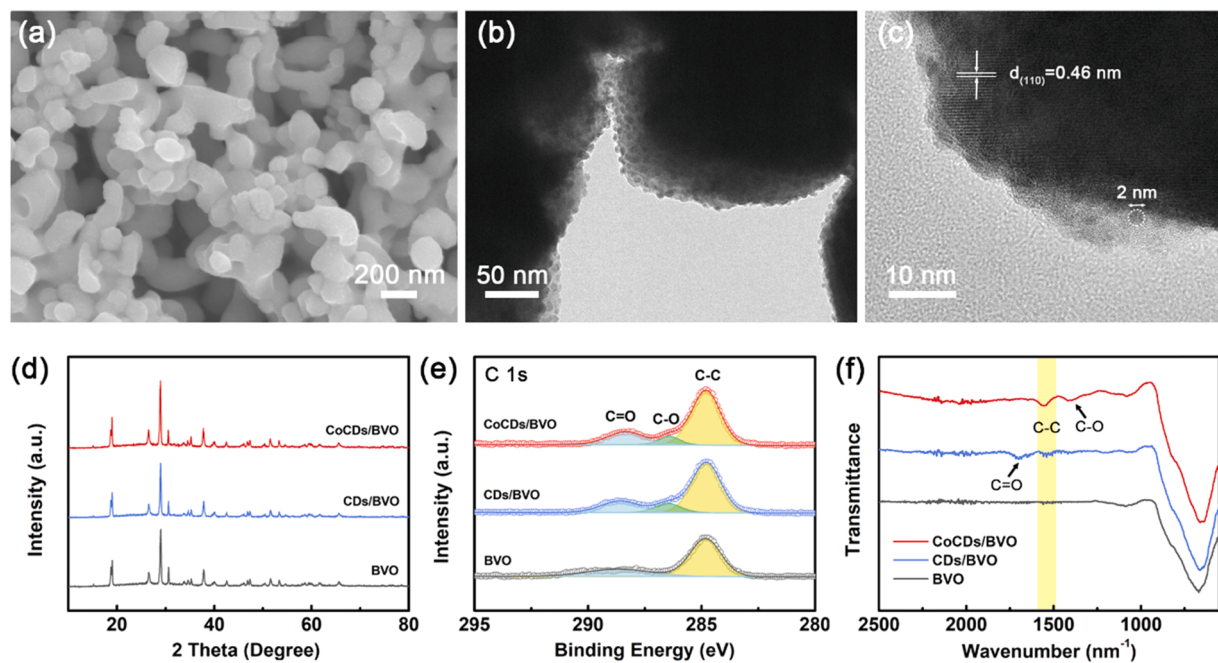


Fig. 2. (a) SEM image, (b) TEM image and (c) HRTEM image of CoCDs/BVO. (d) XRD patterns, (e) high-resolution XPS C 1s spectra and (f) FTIR spectra of BVO, CDs/BVO and CoCDs/BVO photoanodes.

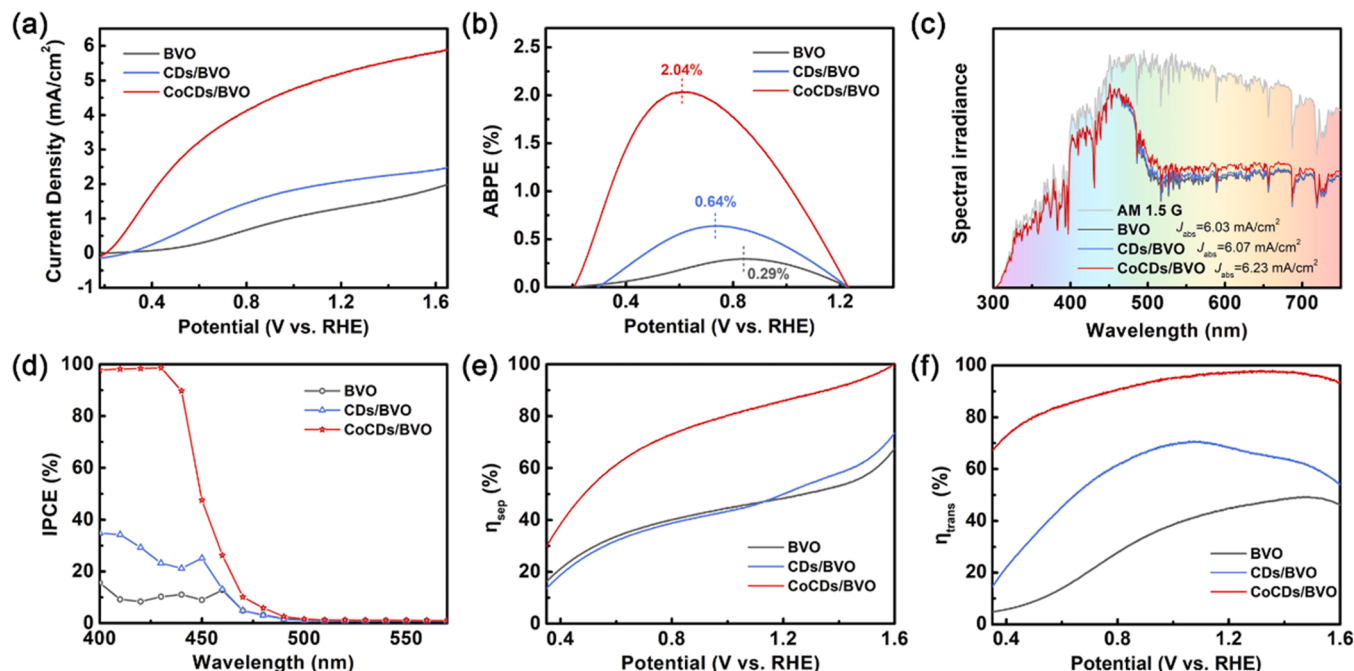


Fig. 3. (a) Photocurrent density versus applied potential curves of BVO, CDs/BVO and CoCDs/BVO photoanodes in 1 M KBr electrolyte. (b) ABPE curves of BVO, CDs/BVO and CoCDs/BVO photoanodes. (c) Spectra of the solar irradiance of AM 1.5 G (ASTM G173-03) and those weighted by the light absorption efficiency of BVO, CDs/BVO and CoCDs/BVO photoanodes. (d) IPCE curves of BVO, CDs/BVO and CoCDs/BVO photoanodes. (e) Charge separation efficiency and (f) charge transfer efficiency of BVO, CDs/BVO and CoCDs/BVO photoanodes.

steps: light absorption, charge separation and surface charge transfer [3]. Therefore, the photocurrent can be expressed as the product of the efficiencies of these steps, i.e., $J = J_{\max} \times \eta_{\text{abs}} \times \eta_{\text{sep}} \times \eta_{\text{trans}}$, where J_{\max} is the theoretical maximum photocurrent density of a semiconductor material ($\sim 7.5 \text{ mA/cm}^2$ for BiVO₄). Light absorption ability change of carbon nanodots coating was first investigated. UV-Vis spectra of all three samples in Fig. S6(a) show a light absorption edge of 500 nm and the Tauc plots in Fig. S6(b) confirms that all the photoanodes have the

same band gap of 2.52 eV. However, CoCDs/BVO exhibits an increased light absorption over 500 nm, which may originate from the additional absorption peak of CoCDs in Fig. 1(h). The unity converted photocurrent density J_{abs} can be calculated by integrating light absorption efficiency with the standard solar spectrum (ASTMG-173-03) according to Eq. (2) in [Supporting Information](#). As shown in Fig. 3(c), when weighted by the light absorption efficiency, the spectral absorption of CoCDs/BVO enhances between 480 nm and 650 nm, thus CoCDs/BVO has a slightly

higher J_{abs} (6.23 mA/cm²) than CDs/BVO (6.07 mA/cm²) and BVO (6.03 mA/cm²).

The incident photon-to-current conversion efficiency (IPCE) varied with wavelength were measured at 1.23 V_{RHE}. The IPCE curve of BVO in Fig. 3(d) reveals that BVO is photo-active at the wavelength below 500 nm, consistent with its band gap of 2.52 eV. CoCDs/BVO exhibits dramatically enhanced IPCE values nearly 100% below 440 nm. What's more, the IPCE of CoCDs/BVO also increase between 450 nm and 500 nm, while the curves of CDs/BVO and BVO almost overlap in this region. The conversion enhancement from photon to current is supposed to result from the photosensitivity of Co-doped carbon nanodots [11].

The charge separation and transfer efficiencies were evaluated to further reveal the function of CoCDs. The LSV curves were recorded in 1 M KBi electrolyte with 0.2 M Na₂SO₃ as a hole scavenger (Fig. S7). The charge separation efficiency η_{sep} and charge transfer efficiency η_{trans} can then be calculated accordingly. As shown in Fig. 3(e) and (f), the coating of CoCDs greatly enhances both η_{sep} and η_{trans} of BiVO₄ photoanodes. CoCDs/BVO reaches a η_{sep} of 86.76% at 1.23 V_{RHE}, while the η_{sep} curve of CDs/BVO overlaps with that of BVO.

The separation efficiency may reflect the heterojunction formation at the carbon nanodots/BVO interface, so Mott-Schottky (MS) curves were measured to investigate the change on band structures. From the MS curves in Fig. 4(a), the overall n-type characteristics of BVO films are maintained after the coating of carbon nanodots. The slopes of three curves are quite similar, thus there is no obvious increase in the charge density. Nevertheless, there is a positive shift of flat-band potential (E_{FB}) upon the coating of CDs, which indicates a possible formation of p-n heterojunction between BVO and CDs [6]. However, the heterojunction did not benefit to charge separation, perhaps because of the large band edge mismatch. Instead, the E_{FB} of CoCDs/BVO sticks to 0.17 V_{RHE}, which can be attributed to the impurity level from CoCDs [37]. The more negative E_{FB} results in larger photovoltage that can be evaluated by the difference of open circuit potential (ΔOCP) under chopped illumination [38] (Fig. S8), which further improves charge separation.

3D charge density difference analysis was performed to analysis the

charge flow at the carbon nanodots/BVO interface. Carbon sheets with 14 hexagonal rings capped with H atoms were constructed to model the CDs and CoCDs (Fig. S9), whose optimized lateral sizes are about 13.7 Å, fitting well with the observation from TEM and AFM. Accordingly, a large supercell of monoclinic BiVO₄ with 216 atoms was built to accommodate with the carbon sheets. As illustrated in Fig. 4(b), the charge density reduces at the CoCDs side while increases at the BVO side, suggesting an electron flow from CoCDs to BVO. Bader charge analysis reveals that 5.07 electrons are transferred from CoCDs to BiVO₄. In contrast, only 4.23 electrons were transferred to BiVO₄ in the CDs/BVO system (Fig. S10).

High-resolution XPS spectra in Fig. 4(c) and (d) also prove the strong electronic interaction between CoCDs and BVO. The characteristic peaks at 163.9 eV and 158.6 eV in the Bi 4f spectrum of BVO can be assigned to the Bi 4f_{5/2} and Bi 4f_{7/2} orbitals, while the peak at 516.2 eV originates from V 2p_{3/2} orbital. All the Bi 4f and V 2p peaks shift to higher binding energy, which can be attributed to strong electron interaction between BiVO₄ and carbon nanodots [39] through oxygen-containing functional groups on the surface. What's more, compared to CDs/BVO, the Bi 4f and V 2p peaks of CoCDs/BVO shift to lower binding energy, indicating that CoCDs can extract holes from BiVO₄ to CoCDs. Based on the above analysis, it can be concluded that upon Co doping, CoCDs serves as a better surface modifier for BiVO₄, so holes flow more effectively from BiVO₄ to CoCDs, which is beneficial for the surface reaction.

3.4. Oxygen evolution reaction (OER) activity of CoCDs

Generally, the charge transfer efficiency η_{trans} refers to the rate of OER reaction at the semiconductor/liquid interface [40]. As illustrated in Fig. 3(f), CoCDs/BVO reaches an ultrahigh η_{trans} of 97.35% at 1.23 V_{RHE}, which implies the excellent OER catalysis ability of CoCDs. LSV curves in dark further demonstrate the excellent OER catalysis activity of CoCDs. The J-V curve of CoCDs/BVO in Fig. S11 shows an obviously reduced onset potential than BVO and CDs/BVO. Linear fitting of the CoCDs/BVO electrode gives a Tafel slope of 168 mV dec⁻¹ (Fig. 5(a)), which is much lower than that of pristine BVO

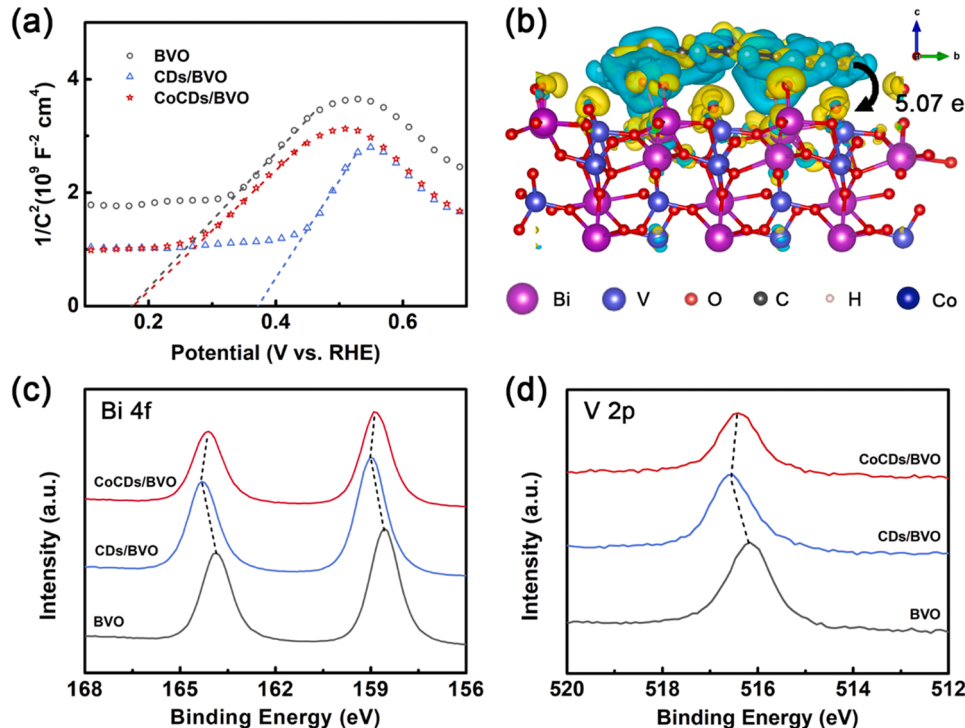


Fig. 4. (a) Mott-Schottky curves of BVO, CDs/BVO and CoCDs/BVO. (b) 3D charge density difference of CoCDs/BVO. (Yellow cloud represents electron accumulation and cyan cloud denotes electron depletion.) High-resolution XPS spectra of (c) Bi 4f and (d) V 2p orbitals of BVO, CDs/BVO and CoCDs/BVO.

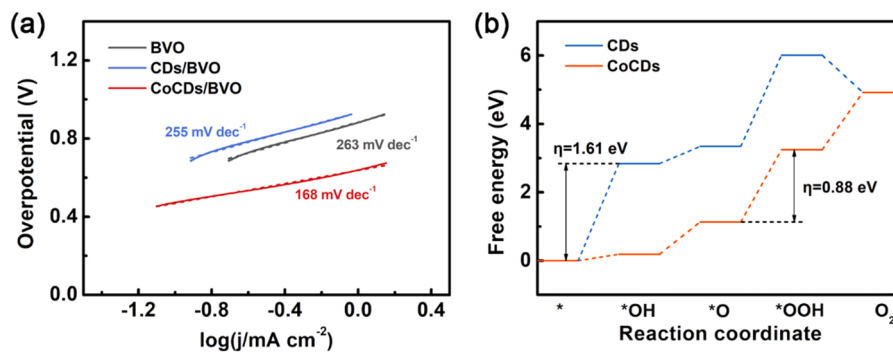


Fig. 5. (a) Tafel plots of BVO, CDs/BVO and CoCDs/BVO. (b) Free-energy diagram of OER pathway on CDs and CoCDs.

(263 mV dec⁻¹) and CDs/BVO (255 mV dec⁻¹).

High-resolution XPS Co 2p spectrum (Fig. S12) was investigated to reveal the chemical states of Co element. The main peak at around 780.0 eV corresponds to Co 2p_{3/2}, which can be fitted to Co³⁺ (780.79 eV), Co²⁺ (782.04 eV) and two satellite peaks (785.46 eV and 788.39 eV) [41]. The co-existence of Co³⁺ and Co²⁺ indicates that Co atoms are embedded into the carbon skeleton because of the in-situ synthesis method. The carbon lattice is an ideal substrate to stabilize metal atoms and promote charge transfer, which is considered as active centers for the reaction [39], thus boosts the activity of Co atoms [34]. To further confirm the hypothesis, DFT calculations were carried out to investigate the OER process on CDs and CoCDs. Typically, an OER process can be divided into four steps [42,43] (Fig. 5(b)). For CDs, the first step (* → *OH) is the rate-determining step and the overpotential is about 1.61 eV. As for CoCDs, the third step (*O → *OOH) becomes the rate-determining one with a low overpotential of 0.88 eV. Electrochemical impedance spectroscopy (EIS) also verifies the promoted charge transfer. As shown in Fig. S13(a), the EIS spectrum of CoCDs/BVO has the smallest semicircle. When fitted by the equivalent circuit in Fig. S13(b), the fitted charge transfer resistance R_{ct} of CoCDs/BVO in Table S3 is much lower than that of BVO, while the series resistance R_s of three samples are similar.

Compared to bare BVO, the charge transfer is also improved by the coating of CDs, which may result from the better hydrophilicity. As shown in Fig. S14, the contact angle decreases from 47.6° of the BVO film to 33.6° of the CDs/BVO film. Such an increased wettability originates from the hydrophilic functional groups on CDs and is beneficial to the adsorption of water molecules onto the active sites [5]. Moreover, the CoCDs/BVO film exhibits an even higher hydrophilicity with a contact angle of 9.0° (Fig. S14(c)), which agrees well with the low energy barrier of the first adsorption step (* → *OH) of CoCDs in Fig. 5(b).

The stability of CoCDs/BVO photoanodes was also evaluated. A stable photocurrent density of CoCDs/BVO is maintained for 4 h under AM 1.5 G illumination at 0.8 V_{RHE} (Fig. S15). As confirmed by XPS, the Co 2p spectra of CoCDs/BVO before and after stability test have similar intensity (Fig. S16). Since the dissolution of metal ions is the main reason for performance decay [20,39], the stability of CoCDs/BVO results from the embedment of Co dopants into the carbon matrix and the anchor effect of surface functional groups. What's more, for better comparison, Co²⁺ was added after the hydrothermal synthesis of CDs and then dropped onto bare BVO electrodes, thus Co ions combined with carbon nanodots only through adsorption. The obtained samples are denoted as Co+CDs/BVO. As shown in Fig. S17, the photocurrent density of Co+CDs/BVO is merely 2.69 mA/cm² at 1.23 V_{RHE}, much lower than CoCDs/BVO, and the photocurrent decay rapidly in 1 h (Fig. S15). Again, it is proved that the carbon framework of carbon nanodots not only activates Co atoms, but also stabilizes them to avoid their dissolution.

Therefore, the water splitting procedure of CoCDs/BVO can be demonstrated as shown in Fig. 6. First, photogenerated holes on the valence band (VB) transfer to the Co impurity level, so their

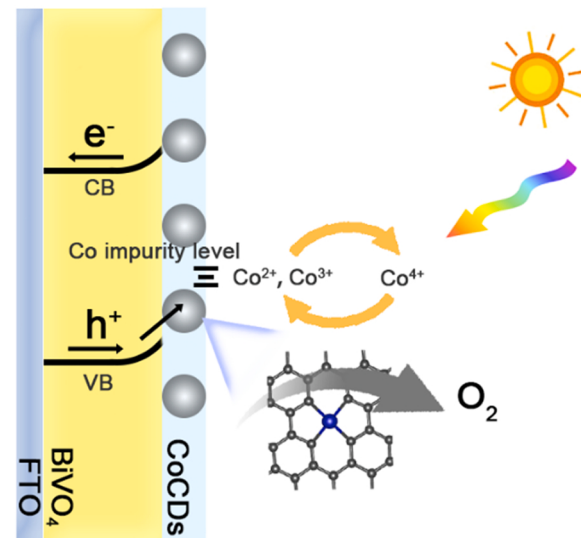


Fig. 6. Schematic illustration of reaction on the CoCDs/BVO photoanodes.

recombination with electrons on the conduction band (CB) is inhibited. In the meantime, the valence change of Co assists holes to participate into water splitting reaction [44,45]. What's more, the graphite carbon matrix can accommodate Co atoms and promote local charge transfer, thus activates and stabilizes the Co atoms, which makes CoCDs/BVO photoanodes efficient and robust.

4. Conclusions

In summary, cobalt-doped carbon nanodots (CoCDs) was designed to boost photoelectrochemical water splitting performance of BiVO₄ photoanodes. The results reveal that CoCDs can not only form heterojunction with BiVO₄ photoanodes, but also greatly promote surface oxygen evolution reaction (OER). The CoCDs/BVO photoanodes exhibit an outstanding photocurrent density of 5.26 mA/cm² at 1.23 V vs. reversible hydrogen electrode (RHE) and good stability because of the simultaneously enhanced charge separation and surface reaction. Detailed investigation reveals that when embedded into carbon nanodots, Co atoms can be stabilized and their OER catalysis activity is greatly boosted, therefore the CoCDs turn out to be an excellent modifier for BiVO₄/liquid interface. Our findings may inspire the exploration of carbon nanomaterials for efficient and robust photoelectrode decoration, as well as the optimization of photoelectrode/liquid interface.

CRediT authorship contribution statement

Jingyi Lin: Investigation, Methodology, Formal analysis,

Visualization, Validation, Writing – original draft. **Runlu Liu**: Investigation, Resources. **Xin Li**: Validation. **Yixin Zhao**: Supervision. **Lingti Kong**: Software, Visualization, Data curation. **Yao Li**: Supervision. **Shenmin Zhu**: Supervision, Conceptualization, Writing – review & editing, Project administration, Funding acquisition. **Lianzhou Wang**: Supervision, Conceptualization, Writing – review & editing.

Declaration of Competing Interest

The authors declare that they have no known competing financial interests or personal relationships that could have appeared to influence the work reported in this paper.

Data availability

Data will be made available on request.

Acknowledgement

The authors kindly acknowledge the financial support from National Natural Science Foundation of China (51672173, U1733130); Shanghai Science and Technology Committee (21ZR1435700, 18520744700, 18JC1410500); Shanghai Jiao Tong University Medical Engineering Cross Research Program (YG2023ZD18). The computations in this paper were run on the Siyuan-1 cluster supported by the Center for High Performance Computing at Shanghai Jiao Tong University.

Appendix A. Supporting information

Supplementary data associated with this article can be found in the online version at [doi:10.1016/j.apcatb.2023.123544](https://doi.org/10.1016/j.apcatb.2023.123544).

References

- [1] C.R. Jiang, S.J.A. Moniz, A.Q. Wang, T. Zhang, J.W. Tang, Photoelectrochemical devices for solar water splitting - materials and challenges, *Chem. Soc. Rev.* 46 (2017) 4645–4660.
- [2] M.G. Walter, E.L. Warren, J.R. McKone, S.W. Boettcher, Q.X. Mi, E.A. Santori, N.S. Lewis, Solar water splitting cells, *Chem. Rev.* 110 (2010) 6446–6473.
- [3] T. Hisatomi, J. Kubota, K. Domen, Recent advances in semiconductors for photocatalytic and photoelectrochemical water splitting, *Chem. Soc. Rev.* 43 (2014) 7520–7535.
- [4] M.F. Licherman, S. Hu, M.H. Richter, E.J. Crumlin, S. Axnanda, M. Favaro, W. Drisdell, Z. Hussain, T. Mayer, B.S. Brunschwig, N.S. Lewis, Z. Liu, H. J. Lewerenz, Direct observation of the energetics at a semiconductor/liquid junction by operando X-ray photoelectron spectroscopy, *Energy Environ. Sci.* 8 (2015) 2409–2416.
- [5] J. Jian, S.Y. Wang, Q. Ye, F. Li, G.R. Su, W. Liu, C.Z. Qu, F. Liu, C. Li, L.C. Jia, A. A. Novikov, V.A. Vinokurov, D.H.S. Harvey, D. Shchukin, D. Friedrich, R. van de Krol, H.Q. Wang, Activating a semiconductor-liquid junction via laser-derived dual interfacial layers for boosted photoelectrochemical water splitting, *Adv. Mater.* 34 (2022) 2201140.
- [6] S.C. Wang, T.W. He, J.H. Yun, Y.X. Hu, M. Xiao, A.J. Du, L.Z. Wang, New iron-cobalt oxide catalysts promoting BiVO₄ films for photoelectrochemical water splitting, *Adv. Funct. Mater.* 28 (2018) 1802685.
- [7] F.M. Toma, J.K. Cooper, V. Kunzelmann, M.T. McDowell, J. Yu, D.M. Larson, N. J. Borys, C. Abelyan, J.W. Beeman, K.M. Yu, J.H. Yang, L. Chen, M.R. Shaner, J. Spurgeon, F.A. Houle, K.A. Persson, I.D. Sharp, Mechanistic insights into chemical and photochemical transformations of bismuth vanadate photoanodes, *Nat. Commun.* 7 (2016) 12012.
- [8] D.K. Lee, K.S. Choi, Enhancing long-term photostability of BiVO₄ photoanodes for solar water splitting by tuning electrolyte composition, *Nat. Energy* 3 (2018) 53–60.
- [9] T.S. Zhou, S. Chen, J.C. Wang, Y. Zhang, J.H. Li, J. Bai, B.X. Zhou, Dramatically enhanced solar-driven water splitting of BiVO₄ photoanode via strengthening hole transfer and light harvesting by co-modification of CQDs and ultrathin beta-FeOOH layers, *Chem. Eng. J.* 403 (2021), 126350.
- [10] X.Y. Zhang, Q.S. Zeng, Y. Xiong, T.J. Ji, C. Wang, X.Y. Shen, M. Lu, H.R. Wang, S. P. Wen, Y. Zhang, X.Y. Yang, X. Ge, W. Zhang, A.P. Litvin, A.V. Baranov, D. Yao, H. Zhang, B. Yang, A.L. Rogach, W.T. Zheng, Energy level modification with carbon dot interlayers enables efficient perovskite solar cells and quantum dot based light-emitting diodes, *Adv. Funct. Mater.* 30 (2020) 1910530.
- [11] K.H. Ye, Z.L. Wang, J.W. Gu, S. Xiao, Y.F. Yuan, Y. Zhu, Y.M. Zhang, W.J. Mai, S. H. Yang, Carbon quantum dots as a visible light sensitizer to significantly increase the solar water splitting performance of bismuth vanadate photoanodes, *Energy Environ. Sci.* 10 (2017) 772–779.
- [12] Y. Liu, B.R. Wygant, K. Kawashima, O. Mabayoje, T.E. Hong, S.G. Lee, J. Lin, J. H. Kim, K. Yubuta, W.Z. Li, J. Li, C.B. Mullins, Facet effect on the photoelectrochemical performance of a WO₃/BiVO₄ heterojunction photoanode, *Appl. Catal., B* 245 (2019) 227–239.
- [13] K.H. Ye, H.B. Li, D. Huang, S. Xiao, W.T. Qiu, M.Y. Li, Y.W. Hu, W.J. Mai, H.B. Ji, S. H. Yang, Enhancing photoelectrochemical water splitting by combining work function tuning and heterojunction engineering, *Nat. Commun.* 10 (2019) 3687.
- [14] X.T. Zheng, A. Ananthanarayanan, K.Q. Luo, P. Chen, Glowing graphene quantum dots and carbon dots: Properties, syntheses, and biological applications, *Small* 11 (2015) 1620–1636.
- [15] W. Li, W. Zhou, Z.S. Zhou, H.R. Zhang, X.J. Zhang, J.L. Zhuang, Y.L. Liu, B.F. Lei, C.F. Hu, A universal strategy for activating the multicolor room-temperature afterglow of carbon dots in a boric acid matrix, *Angew. Chem.* 58 (2019) 7278–7283.
- [16] T.X. Chen, T.T. Yao, H. Peng, A.K. Whittaker, Y. Li, S.M. Zhu, Z.Y. Wang, An injectable hydrogel for simultaneous photothermal therapy and photodynamic therapy with ultrahigh efficiency based on carbon dots and modified cellulose nanocrystals, *Adv. Funct. Mater.* 31 (2021) 2106079.
- [17] Y. Guo, R. Zhang, S.C. Zhang, H. Hong, Y.W. Zhao, Z.D. Huang, C.P. Han, H.F. Li, C. Y. Zhi, Ultrahigh oxygen-doped carbon quantum dots for highly efficient H₂O₂ production via two-electron electrochemical oxygen reduction, *Energy Environ. Sci.* 15 (2022) 4167–4174.
- [18] J. Liu, S.Y. Zhao, C.X. Li, M.M. Yang, Y.M. Yang, Y. Liu, Y. Lifshitz, S.T. Lee, Z. H. Kang, Carbon nanodot surface modifications initiate highly efficient, stable catalysts for both oxygen evolution and reduction reactions, *Adv. Energy Mater.* 6 (2016) 1502039.
- [19] J.H. Wang, W. Cui, Q. Liu, Z.C. Xing, A.M. Asiri, X.P. Sun, Recent progress in cobalt-based heterogeneous catalysts for electrochemical water splitting, *Adv. Mater.* 28 (2016) 215–230.
- [20] L.S. Peng, N. Yang, Y.Q. Yang, Q. Wang, X.Y. Xie, D. Sun-Waterhouse, L. Shang, T. R. Zhang, G.I.N. Waterhouse, Atomic cation-vacancy engineering of NiFe-layered double hydroxides for improved activity and stability towards the oxygen evolution reaction, *Angew. Chem.* 60 (2021) 24612–24619.
- [21] W.J. Lu, Y.J. Guo, J.H. Zhang, Y.F. Yue, L. Fan, F. Li, C. Dong, S.M. Shuang, A high catalytic activity nanzyme based on cobalt-doped carbon dots for biosensor and anticancer cell effect, *ACS Appl. Mater. Interfaces* 14 (2022) 57206–57214.
- [22] T.L. Feng, G.T. Yu, S.Y. Tao, S.J. Zhu, R.Q. Ku, R. Zhang, Q.S. Zeng, M.X. Yang, Y. X. Chen, W.H. Chen, W. Chen, B. Yang, A highly efficient overall water splitting ruthenium-cobalt alloy electrocatalyst across a wide pH range via electronic coupling with carbon dots, *J. Mater. Chem. A* 8 (2020) 9638–9645.
- [23] T.W. Kim, K.S. Choi, Nanoporous BiVO₄ photoanodes with dual-layer oxygen evolution catalysts for solar water splitting, *Science* 343 (2014) 990–994.
- [24] G. Kresse, J. Furthmuller, Efficient iterative schemes for ab initio total-energy calculations using a plane-wave basis set, *Phys. Rev. B* 54 (1996) 11169–11186.
- [25] J.K. Norskov, J. Rossmeisl, A. Logadottir, L. Lindqvist, J.R. Kitchin, T. Bligaard, H. Jónsson, Origin of the overpotential for oxygen reduction at a fuel-cell cathode, *J. Phys. Chem. B* 108 (2004) 17886–17892.
- [26] V. Wang, N. Xu, J.C. Liu, G. Tang, W.T. Geng, VASPKIT: A user-friendly interface facilitating high-throughput computing and analysis using VASP code, *Comput. Phys. Commun.* 267 (2021).
- [27] S. Grimme, J. Antony, S. Ehrlich, H. Krieg, A consistent and accurate ab initio parametrization of density functional dispersion correction (DFT-D) for the 94 elements H–Pu, *J. Chem. Phys.* 132 (2010), 154104.
- [28] Y.Q. Dong, J.W. Shao, C.Q. Chen, H. Li, R.X. Wang, Y.W. Chi, X.M. Lin, G.N. Chen, Blue luminescent graphene quantum dots and graphene oxide prepared by tuning the carbonization degree of citric acid, *Carbon* 50 (2012) 4738–4743.
- [29] Z. Xu, C. Gao, Aqueous liquid crystals of graphene oxide, *ACS Nano* 5 (2011) 2908–2915.
- [30] X. Miao, D. Qu, D.X. Yang, B. Nie, Y.K. Zhao, H.Y. Fan, Z.C. Sun, Synthesis of carbon dots with multiple color emission by controlled graphitization and surface functionalization, *Adv. Mater.* 30 (2018) 1704740.
- [31] S.J. Zhu, J.R. Shao, Y.B. Song, X.H. Zhao, J.L. Du, L. Wang, H.Y. Wang, K. Zhang, J. H. Zhang, B. Yang, Investigating the surface state of graphene quantum dots, *Nanoscale* 7 (2015) 7927–7933.
- [32] B.S. Tian, S.K. Liu, L.L. Feng, S.H. Liu, S.L. Gai, Y.L. Dai, L.S. Xie, B. Liu, P.P. Yang, Y.L. Zhao, Renal-clearable nickel-doped carbon dots with boosted photothermal conversion efficiency for multimodal imaging-guided cancer therapy in the second near-infrared biowindow, *Adv. Funct. Mater.* 31 (2021) 2100549.
- [33] J. Peng, W. Gao, B.K. Gupta, Z. Liu, R. Romero-Aburto, L.H. Ge, L. Song, L. B. Alemany, X.B. Zhan, G.H. Gao, S.A. Vithayathil, B.A. Kaipparettu, A.A. Marti, T. Hayashi, J.J. Zhu, P.M. Ajayan, Graphene quantum dots derived from carbon fibers, *Nano Lett.* 12 (2012) 844–849.
- [34] Q. Wang, J. Li, X.J. Tu, H.B. Liu, M. Shu, R. Si, C.T.J. Ferguson, K.A.I. Zhang, R. Li, Single atomically anchored cobalt on carbon quantum dots as efficient photocatalysts for visible light-promoted oxidation reactions, *Chem. Mater.* 32 (2020) 734–743.
- [35] Z.X. Gan, H. Xu, Y.L. Hao, Mechanism for excitation-dependent photoluminescence from graphene quantum dots and other graphene oxide derivatives: consensus, debates and challenges, *Nanoscale* 8 (2016) 7794–7807.
- [36] D.Z. Yao, C. Tang, A. Vasilieff, X. Zhi, Y. Jiao, S.Z. Qiao, The controllable reconstruction of Bi-MOFs for electrochemical CO₂ reduction through electrolyte and potential mediation, *Angew. Chem.* 60 (2021) 18178–18184.
- [37] S.C. Wang, P. Chen, J.H. Yun, Y.X. Hu, L.Z. Wang, An electrochemically treated BiVO₄ photoanode for efficient photoelectrochemical water splitting, *Angew. Chem.* 56 (2017) 8500–8504.

[38] Q. Sun, T. Cheng, Z.R. Liu, L.M. Qi, A cobalt silicate modified BiVO_4 photoanode for efficient solar water oxidation, *Appl. Catal., B* 277 (2020), 119189.

[39] J.Y. Lin, X.J. Han, S.Y. Liu, Y. Lv, X. Li, Y.X. Zhao, Y. Li, L.Z. Wang, S.M. Zhu, Nitrogen-doped cobalt-iron oxide cocatalyst boosting photoelectrochemical water splitting of BiVO_4 photoanodes, *Appl. Catal., B* 320 (2023), 121947.

[40] L. Liardet, J.E. Katz, J.S. Luo, M. Gratzel, X.L. Hu, An ultrathin cobalt-iron oxide catalyst for water oxidation on nanostructured hematite photoanodes, *J. Mater. Chem. A* 7 (2019) 6012–6020.

[41] L. Xu, Q.Q. Jiang, Z.H. Xiao, X.Y. Li, J. Huo, S.Y. Wang, L.M. Dai, Plasma-engraved Co_3O_4 nanosheets with oxygen vacancies and high surface area for the oxygen evolution reaction, *Angew. Chem.* 55 (2016) 5277–5281.

[42] J. Rossmeisl, A. Logadottir, J.K. Norskov, Electrolysis of water on (oxidized) metal surfaces, *Chem. Phys.* 319 (2005) 178–184.

[43] J. Rossmeisl, Z.W. Qu, H. Zhu, G.J. Kroes, J.K. Norskov, Electrolysis of water on oxide surfaces, *J. Electroanal. Chem.* 607 (2007) 83–89.

[44] S.Q. Zhou, K.Y. Chen, J.W. Huang, L. Wang, M.Y. Zhang, B. Bai, H. Liu, Q.Z. Wang, Preparation of heterometallic CoNi -MOFs-modified BiVO_4 : a steady photoanode for improved performance in photoelectrochemical water splitting, *Appl. Catal., B* 266 (2020), 118513.

[45] C.C. Feng, Q. Zhou, B. Zheng, X. Cheng, Y.J. Zhang, Y.P. Bi, Ultrathin NiCo_2O_4 nanosheets with dual-metal active sites for enhanced solar water splitting of a BiVO_4 photoanode, *J. Mater. Chem. A* 7 (2019) 22274–22278.